

Research Article

Ultrasound-Based Three-Dimensional Microangiography for Repeated Noninvasive Imaging of Neovascularization

Fredrik K. E. Guldbæk-Svensson,¹ Mathias M. Thygesen,¹ Teresa H. Nielsen,¹
Trine W. Mikkelsen,¹ Ming Ding ,^{2,3} Michael Pedersen ,¹ and Henrik Lauridsen ¹

¹Department of Clinical Medicine, Aarhus University, 8200 Aarhus N, Aarhus, Denmark

²Orthopaedic Research Laboratory, Department of Orthopaedic Surgery & Traumatology, Odense University Hospital, 5000 Odense C, Odense, Denmark

³Department of Clinical Research, University of Southern Denmark, 5000 Odense C, Odense, Denmark

Correspondence should be addressed to Henrik Lauridsen; henrik@clin.au.dk

Received 10 June 2022; Revised 12 October 2022; Accepted 29 October 2022; Published 18 January 2023

Academic Editor: Anne Roivainen

Copyright © 2023 Fredrik K. E. Guldbæk-Svensson et al. This is an open access article distributed under the Creative Commons Attribution License, which permits unrestricted use, distribution, and reproduction in any medium, provided the original work is properly cited.

Neovascularization plays an essential part in the progression of several diseases as well as recovery processes such as angiogenesis-guided neurogenesis after a spinal cord injury. To visualize and quantify neovascularization in an experimental setup, it is desirable to apply a noninvasive, repeatable, and harmless technique. Here, we apply a newly developed ultrasound-based technique to construct angiographies and quantify neovascularization in the regenerating spinal cord of a regeneration competent animal model, the Mexican axolotl. We measured vessel volume fraction prior to the induction of contusion and transection spinal cord injury and repeated this measurement directly after injury and at 3, 6, 12, and 63 days after injury. Although neither of the injury types resulted in statistically significant differences in vessel volume fraction relative to sham-operated animals, there was a statistically significant increase in neovascularization over time in all groups. Additionally, vessel volume fraction at the final time point (63 days after injury) was quantified with micro-CT imaging after vascular perfusion with a contrast agent, confirming no statistically significant difference in neovascularization between injury types. Ex vivo vessel volume fraction measured by micro-CT was significantly different from the in vivo ultrasound-based measurement at the same time point. This is likely a result of incomplete vascular perfusion with the contrast agent before micro-CT imaging, which was supported by subsequent histological evaluation. In summary, the results suggest that the ultrasound-based angiographic procedure, we demonstrate here, is applicable to visualize and quantify neovascularization in a noninvasive and harmless fashion in longitudinal experiments circumventing the limitations of contrast agent-dependent techniques.

1. Introduction

Deep tissue neovascularization can be visualized and quantified in three-dimensional (3D) space by several imaging techniques, such as ultrasound and CT angiography. Ultrasound imaging reveals blood flow dynamics in deep tissue, and it is applicable in longitudinal experiments to evaluate the ingrowth of new vasculature. However, traditional brightness mode (B-mode) ultrasound has a relatively low signal-to-noise ratio compared with micro-CT of contrast agent perfused vessels, and Doppler-based ultrasound techniques (e.g., color Doppler and power Doppler) are limited by their inability to visualize vessels that run in a direction

perpendicular to the ultrasound propagation. Recently, a novel ultrasound postprocessing procedure was developed by Tan et al. [1] and Dittrich et al. [2] and further refined by Damsgaard and Lauridsen [3], relying on the fact that blood signal in animals with nucleated red blood cells (RBCs) (all vertebrate animals except postnatal mammals) in B-mode images has a more dynamic speckle pattern than soft tissue. By calculating the quadratic average (i.e., finding the standard deviation on a pixel-by-pixel level), a stack of B-mode images (a cine stack) can be compressed to a single frame with a much higher signal-to-noise ratio than individual B-mode images. This concept allows for enhanced signal-to-noise ratio and a full 3D acquisition using a

step-and-record procedure, and it facilitates deep angiographic imaging generated by high-frequency ultrasound, acquisition with spatial resolutions in the submillimeter range (comparable to micro-CT), and the possibility of repeated, noncontrast based, and noninvasive evaluation over the course of an experiment. The nature of this method provides a new efficient way to construct angiographies repeatedly and noninvasively, which could become useful in several research areas.

In the field of spinal cord injury (SCI) research, a field that focuses on understanding and alleviating the devastating effects of traumatic SCI caused by, e.g., traffic accidents and falls that may lead to complete and permanent loss of neurologic function distal to the injury site [4–9], raising evidence suggests that neural regeneration after a SCI is highly dependent on neovascularization of the injury zone [10–12]. Recent studies have shown that enhanced angiogenesis is associated with increased neurogenesis at the injury site, accelerating recovery of neurologic function, and it has been advocated that the microvascular network may provide an effective “bridge” across the injury cavity, which supports and guides axonal regeneration [10–12]. Furthermore, after acute injury to the central nervous system, immature neuronal migration and axonal sprouting occur along newly formed vessels in perilesional tissue, indicating a close association between angiogenesis and neurogenesis in areas undergoing active neural tissue remodeling [13, 14]. Notably, increased recruitment of neural progenitors to the lesion site has been observed, and these progenitors were closely associated with the distributed blood vessels [10]. Thus, repeated vascular mapping with ultrasound could provide informative *in vivo* images of the neovascularization at the SCI site of the same animal throughout a SCI recovery.

To our knowledge, the association between neurogenesis and neovascularization has only been studied in rodents. To advance our knowledge of this association, it could be valuable to investigate a model capable of complete spinal cord regeneration after injury. Traditional mammalian models in biomedical research do not possess this potential; therefore, to find the closest tetrapod relative with a pronounced regenerative potential, we must look outside our own mammalian class toward the amphibians. The Mexican axolotl (*Ambystoma mexicanum*), a caudate amphibian (salamander), is well established as a laboratory animal and is renowned for its tissue regenerative potential [15–18]. Thus, we selected the axolotl as a model to study the ingrowth of new vessels in a regenerative zone such as the injured spinal cord.

By applying a clinically relevant SCI model that we have previously developed in the axolotl [19], we here aim to: first, test the feasibility of the novel ultrasound angiography procedure for visualization of neovascularization at the injury site in axolotls subjected to transection or contusion SCI. Second, to investigate the relationship between the signal intensity in quadratic averaged B-mode ultrasound cine stacks and blood flow velocities, evaluating the potential to generate flow velocity maps using the ultrasound procedure. Third, to compare quantitative ultrasound end-point measurements of neovascularization with contrast agent-enhanced micro-CT measurements.

2. Materials and Methods

2.1. Ethics Statement. All animal experiments and housing facilities were in accordance with Danish legislation and approved by the Danish Animal Experiments Inspectorate (protocol# 2015-15-0201-00615).

2.2. Animals and Husbandry. Neotenic albino axolotls were purchased (Exoterra, Holzheim, Germany) and housed in individual plastic containers ($39 \times 28 \times 14 \text{ cm}^3$) filled with tap water in a 20°C temperature-controlled environment and exposed to a 12:12 hr light–dark cycle. To ensure that they exhibited full functionality and well-being before intervention and during follow-up, they were observed while stabled every second day, provided food (trout pellets) $\times 3/\text{week}$, and the water was exchanged $\times 1/\text{week}$. Prior to the experiment, the mean \pm standard deviation of body mass and total length was $14.3 \pm 2.3 \text{ g}$ and $12.8 \pm 1.8 \text{ cm}$.

2.3. Surgical Procedures. Eighteen axolotls were randomized to receive transection SCI (TSCI, $n = 6$), contusion SCI (CSCI, $n = 6$), or sham ($n = 6$). One day before surgery, ultrasound was performed, and food was withdrawn for the following week. The surgeon was blinded to animal ID during surgery. In preparation for surgery, the axolotl was transferred to an anesthetic solution containing benzocaine (200 mg/l) and was fully anesthetized after ~ 15 min. Next, the animal was placed in the prone position and wrapped in moist paper wipes soaked in anesthetic solution. A vertical incision was placed bilaterally on the dorsal side of the tail immediately caudal to the anus. The incision continued ventrally to a level just above the vertebrae. A lateral incision was added in the caudal direction bilaterally, and the keel was momentarily flipped from the surgical site to allow access to underlying structures. The paravertebral muscles were released from the vertebrae, and the spinous process of two vertebrae was exposed. Next, laminectomy was performed at two levels to expose the spinal cord. Subsequently, the axolotl received one of following interventions: (1) CSCI: a 25 g metal rod with a 2 mm diameter was released in 30 mm free fall on the exposed spinal cord. An immediate intramedullary hemorrhage was observed verifying successful injury; (2) TSCI: 2 mm transection of the spinal cord using microscissors. A 2 mm clearly visible disruption of the spinal cord was confirmed as part of successful injury; and (3) sham: proceeded directly to the closing procedure. For all axolotls, the wound was closed in one dermatome layer using a Monosof 9-0 suture. Figure 1(a) shows the TSCI and CSCI procedures. After injury, the axolotls were kept at a lower water level for 12 days to minimize vertical movements and use of the tail to reach the surface for air breathing during the healing process.

2.4. High-Frequency Ultrasound Imaging. Ultrasound imaging was performed using a Vevo2100 ultrasound system (FUJIFILM VisualSonics, Toronto, Canada) and a MS550D transducer with a center frequency of 40 MHz. Ultrasound images of the SCI site were acquired one day before and immediately after surgery, 3 days postinjury (3 DPI), 6, 12, and 63 DPI. For 3D acquisition, transducer movements were controlled with

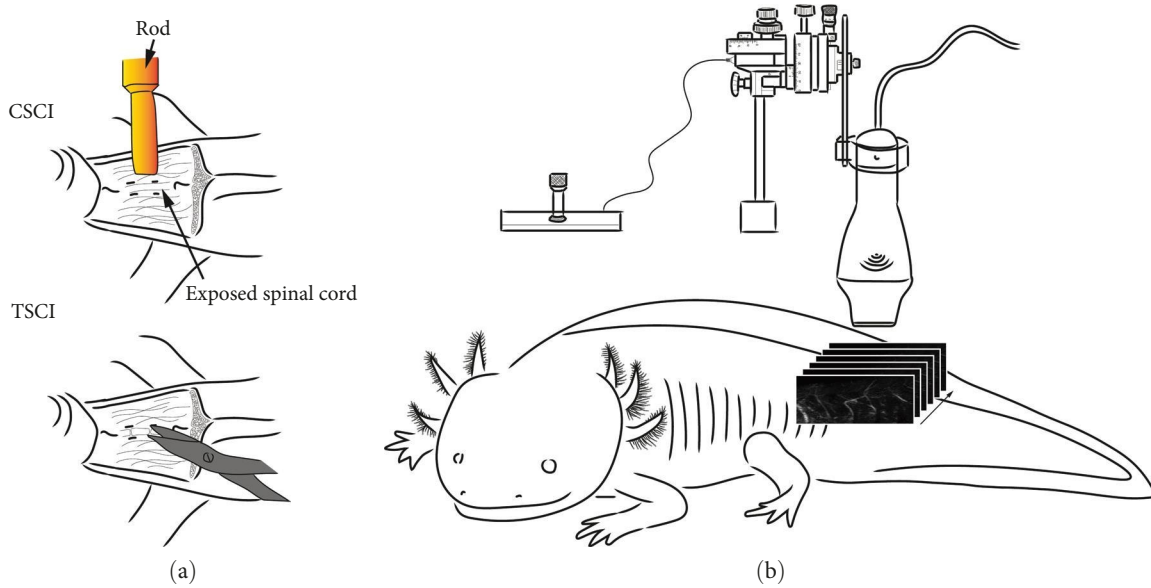


FIGURE 1: Illustration of the SCI models, and high-frequency ultrasound imaging setup: (a) the exposed spinal cord is either injured by a contusion trauma (falling rod) or a transection injury using a microscissor; (b) the high-frequency ultrasound setup with a remote joystick connected to a micromanipulator, which holds the ultrasound transducer. Ultrasound images were obtained according to the direction of the arrow.

an electronic micromanipulator (Brock & Michelsen) operated by a remote joystick. After complete anesthesia was reached, the axolotl was submerged in a prone position into a small container filled with anesthetic solution, and the animal was fixed with sandbags. The tip of the transducer was aligned with the axolotl's long axis and submerged into the benzocaine solution until localized only a few mm above the keel behind the hind limbs of the axolotls. Before injury, the location of surgical intervention was defined as the two vertebrae just caudal to the hind limbs. After injury, the injury site was easily recognizable due to the missing spinous processes. In both cases, the image window was optimized after indentifying the SCI site by adjusting ultrasound settings. Ultrasound images covering the SCI site were acquired in B-mode at multiple sagittal cross-sectional slice locations, with consecutive slices with an interslice interval of $50\ \mu\text{m}$. At each location, cine images containing 500 frames were acquired with a frame rate of ~ 50 frames/s and a transducer frequency of 40 MHz. Figure 1(b) shows the scanning procedure. After each scan, the water in the housing containers was exchanged to reduce the risk of wound infection during the healing process.

2.5. Ultrasound Flow Phantom Casting and Imaging. An ultrasound flow phantom was constructed to correlate measured signal intensities obtained from quadratic averaged B-mode ultrasound with known flow velocities. One circular Styrofoam cup was used as a mold. The mold was perforated in each side and a 0.58 mm catheter was placed across the mold by pushing it through the holes. Subsequently, powdered gelatin was dissolved in deionized water (5 g/l) and left to solidify in the mold at 4°C . As a replacement for axolotl blood that is difficult to obtain in large quantities, a 5 ml blood sample from a sacrificed Atlantic cod (*Gadus morhua*)

was applied as flow medium due to similar ultrasound properties of amphibian and fish blood, both containing nucleated RBCs. The flow phantom catheter was connected to a 5 ml syringe placed in a perfusion pump (Harvard Apparatus, PHD 2000 Infusion). The ultrasound gain was set to 30 dB, and the catheter was perfused with blood at increasing flow velocities: 15.85, 31.7, 47.55, 63.4, 95.1, 126.8, 190.2, 252.6, 378.9, and 507.2 mm/min. At each flow velocity level, 1,000 frames were stored as a cine-image stack for subsequent postprocessing analyses.

2.6. Contrast Agent-Based Micro-CT Imaging. At experimental end point (63 DPI), the same axolotls as used in the in vivo ultrasound experiment were prepared for micro-CT. After being fully anesthetized, each axolotl was moved to a petri dish, containing benzocaine solution. The axolotls were placed in a supine position and fixed with soaked paper towels. A thoracotomy was performed to expose the heart. One or two ligatures were placed unbound behind the outflow tract. A couple droplets of heparinized amphibian Ringer's solution (100 IU/ml) were dripped on the outflow tract surface to prevent coagulation immediately after incision. A cut halfway through the outflow tract was made, followed by insertion of a PE-160 catheter (1.57/1.14 mm outer/inner diameter) connected to a syringe with heparinized amphibian Ringer's solution. Subsequently, the ligatures were bound to the outflow tract, containing the catheter, and the cardiovascular system was rinsed from blood with continuous anterograde perfusion (Harvard Apparatus, PHD 2000 Infusion) with ~ 2 ml heparinized amphibian Ringer's solution, with a flow of $\sim 300\ \mu\text{l}/\text{min}$. Successful removal of the circulatory blood was characterized by effective decoloration of the gills and subdermal vessels. Then, the components of a yellow silicone contrast agent (Microfil MV-122; Flow Tech,

MA, USA) were mixed according to the manufacturer's specification (compound/diluent/curing agent: 1/2/0.3) and aspirated into a syringe. Next, the syringe was connected to the catheter, and the axolotl was filled antegrade with microfil using a volume of twice the estimated blood volume ($\sim 5.5\%$ body volume $\approx 5.5\%$ body mass for an animal of approximate neutral buoyancy) with a flow rate of $300 \mu\text{l}/\text{min}$. Successful perfusion of the circulatory blood system was confirmed by yellow coloring of the gills, subdermal vessels, and heart. After ~ 90 min, the microfil had solidified, and the animal was fixed in 4% formaldehyde (phosphate buffered) at 4°C until micro-CT was scheduled (at least 24 hr after the preparation procedure). A piece of tissue containing the SCI site was harvested prior to the micro-CT examination. Micro-CT was performed using a Scanco Medical $\mu\text{CT}50$ system (Scanco Medical, Brüttisellen, Switzerland) with 2,000 projections/ 180° , an isotropic voxel size of $5 \mu\text{m}$, an X-ray tube voltage of 90 kVp, an X-ray tube current of $155 \mu\text{A}$, and an integration time of 1,000 ms and applying a 0.5 mm aluminum filter. Subsequently, six samples (two from each group) were rescanned with diffusible iodine-based contrast-enhanced CT (diceCT) to evaluate neurogenesis and potential anatomical differences in the spinal cord between groups. These samples were submerged into Lugol's solution (8.3 g/l I_2 and 16.6 g/l KI in deionized water) for 13 ± 1 days prior to scanning and were scanned with the same parameters as described above except with an isotropic voxel size of $7 \mu\text{m}$.

2.7. Histology. At experimental end point (63 DPI), after microfil contrast agent-enhanced micro-CT, three samples (one from each group) were prepared for histology to qualitatively describe potential differences in the spinal cord and related vessels between group. The formaldehyde-fixed tail samples were decalcified 1 hr in 1 M HCl before they were dehydrated in an ethanol series (70%, 96%, 99.9%), cleared in xylene and embedded in paraffin, and sectioned at $4 \mu\text{m}$ thickness along the sagittal axis. Additionally, samples slightly caudal to the injury site were sectioned along the transversal axis to evaluate the level of microfil infusion in blood vessels. All sections were stained with hematoxylin and eosin.

2.8. Clinical Neurologic Examination. Clinical neurologic examination was performed before surgery and at 3, 6, 12, 46, and 63 DPI. The tail caudal to the injury was stimulated with both tactile (gentle touch with forceps) and nociceptive stimuli (forceps pinching). For both stimuli, three attempts were conducted, with the maximum response defining the score of the test: 0 point: no response; 1 point: local tail movement; 2 points: truncal movement; 3 points: coordinated movement of limbs and/or head alongside with truncal movement; and 4 points: immediate coordinated fast movement. The tests were filmed and scored after experimental end point. The scorer was blinded to allocated injury and DPI.

2.9. Image Processing

2.9.1. Construction of Angiographies. Ultrasound cine images were exported as a stack of Dicom-formatted images and processed in ImageJ (version 1.52h) [20]. Each Dicom image represented a sagittal cross-sectional slice with 500 or 1,000

frames at one time point. Each pixel's quadratic mean intensity, $D(x, y)$, was computed over the 500 or 1,000 frames, according to the formula:

$$D(x, y) = \left[\frac{1}{N} \sum_{t=1}^N ((I_t(x, y, t) - \bar{I}(x, y, t))^2) \right]^{1/2}, \quad (1)$$

where $I_t(x, y)$ is the intensity of the pixel at (x, y) pixel coordinate and $\bar{I}(x, y)$ is the arithmetic mean value of I over time. To automate this process, every cine image containing 500 or 1,000 frames was processed in batch mode in ImageJ with a macrosript provided in Script S1.

In the resulting images, pixels with highly dynamic intensities over time (pixels located in blood vessels) appeared bright, while those with low dynamics (pixels located in static soft tissue) appeared dim.

2.9.2. Flow Map Calculations. The angiographies of the flow phantom were used to make gray value measurements. Circular regions of interest (ROI) were placed at different locations in the catheter lumen. Because of the different flows in the catheter wall and center, ROIs were placed at four different locations: in the top, in the middle, in the bottom, and covering the whole catheter lumen. Subsequently, the mean ROI pixel values were calculated and correlated with measured flow rates.

2.9.3. Vessel Volume Fraction Calculations. Ultrasound, micro-CT, and transversal histology images were used to calculate vessel volume fractions. Within each image sequence, the images containing the spinal cord blood vessels were manually included, and the rest were excluded. Ultrasound images with observed artifacts or significant noise were excluded. Artifacts included vibrations and shadowing of the ultrasound beams caused by dense bone structures and sutures. Across the stack of images, a 4 mm long segmented line, 0.8 mm wide, following the injury anteriorly, was drawn and converted into an area, resulting in a 3D ROI. All pixel values inside the 3D ROI were used for histogram analysis. The grayscale values in the images were analyzed, and after extensive piloting to detect pixels that unequivocally belonged to either vessels or soft tissue, it was defined that pixels with signal values >2.1 for quadratic averaged ultrasound images and $>3,500$ for micro-CT images were assigned to vessel lumen, and pixels with signal values ≤ 2.1 for ultrasound and $\leq 3,500$ for micro-CT were assigned to soft tissue. The vessel volume fraction in the 3D ROIs was calculated by dividing the number of pixels with those having values >2.1 for ultrasound and $>3,500$ for micro-CT, with the number of pixels with values ≤ 2.1 for ultrasound and $\leq 3,500$ for micro-CT.

2.10. Statistics. Statistical analyses were performed in IBM SPSS Statistics for Macintosh, version 25.0. Subsequent to testing for normality of distribution and homogeneity of variance, relevant types of t -tests (paired/unpaired, one-/two-tailed) were applied to test for statistically significant differences between two groups, and relevant types of ANOVAs (repeated measure/mixed model, one-way/two-way) were applied for

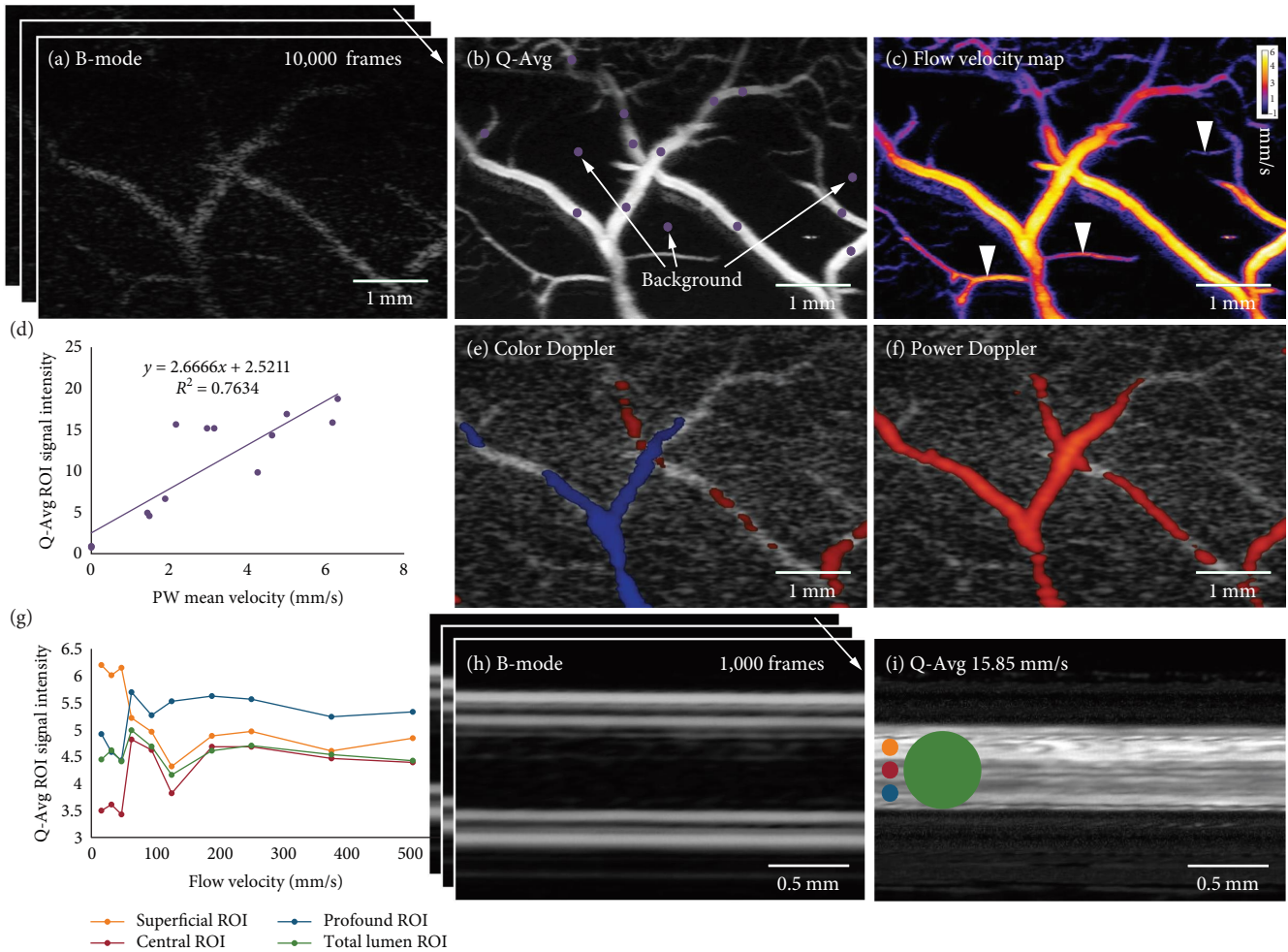


FIGURE 2: Quadratic averaging (Q-Avg) to enhance blood signal in B-mode ultrasound images: (a) stack of traditional B-mode images revealing some vessel structures with a relatively low signal-to-noise ratio; (b) Q-Avg results in blood-enhanced angiography; (c) flow velocity map generated from correlation between signal intensity at selected points (shown as purple dots in (b)) and flow velocity measured at the same positions with pulsed wave Doppler; (d) correlation plot; (e and f) color and power Doppler imaging allow for flow mapping with less sensitivity than quadratic averaging and these techniques are unable to reveal flow perpendicular to the sound direction (compared with arrowheads in (c)); (g) flow phantom measurements showed no statistically significant correlation between signal intensity in quadratic averaged frames and flow velocity in spite that this was indicated on in vivo measurements (d); (h) stack of B-mode images revealing the flow phantom catheter; (i) Q-Avg of the B-mode images obtained at a perfusion speed of 15.85 mm/s. Orange circle: superficial ROI. Red circle: central ROI. Blue circle: Profound ROI. Green circle: total lumen ROI.

omnibus testing of statistically significant difference between more than two groups.

3. Results and Discussion

3.1. Ultrasound-Based Angiography and Flow Velocity Mapping. An initial experiment to construct a blood flow-enhanced angiography in the keel of the axolotl tail using quadratic averaging demonstrated that the technique increased the signal-to-noise ratio of small blood vessels compared to B-mode images (Figures 2(a) and 2(b)). This was largely unaffected by small differences in gain and in ultrasound background scatter. Additionally, in contrast to Doppler-based ultrasound imaging techniques, it allowed for the visualization of vessels running perpendicular to the direction of the ultrasound wave (compare Figure 2(b) with Figures 2(e) and 2(f)). Notably, the signal magnitude in

blood vessels in the quadratic averaged image intuitively seemed to relate to flow velocity. This observation was supported by correlation analysis, as demonstrated in Figure 2(d). This proposed relationship was further investigated in a flow velocity controlled setup with a catheter being perfused by fish blood that has ultrasound characteristics similar to amphibian blood. This experiment showed that there is no statistically significant correlation between signal intensity on quadratic averaged angiographies and flow velocity (Figure 2(g)–2(i)), thus only angiographies were produced in the subsequent experiments.

3.2. Effect of Duration of Benzocaine Anesthesia on Blood Flow in Peripheral Blood Vessels. It has been shown that benzocaine-induced anesthesia affects the central cardiovascular system in the axolotl in a time and anesthesia level-dependent manner [21]. An addendum experiment was

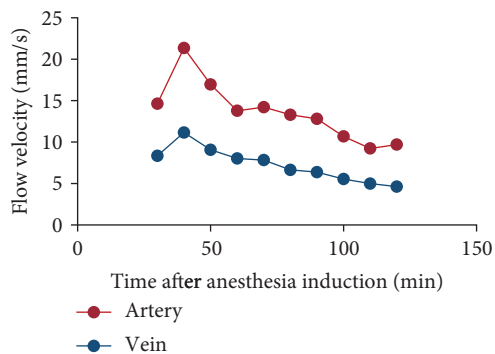


FIGURE 3: Flow velocity alterations in the artery (red) and vein (blue) 30–120 min after onset of benzocaine-induced anesthesia.

conducted on one axolotl to confirm the importance of selecting the same anesthesia level throughout the experiments in flow velocity measurements in peripheral vessels. Peripheral vessels in the tail keel were selected due to the inaccessibility of spinal cord vessels through the intact spine. After being fully anesthetized, the axolotl was moved and fixed using the same procedure, as previously described. The keel just behind the hind limbs was localized by ultrasound, and one artery and one vein were identified. The flow rates in the two vessels were measured with pulsed-wave Doppler mode after 30, 40, 50, 60, 70, 80, 90, 100, 110, and 120 min following onset of anesthesia. The measured flow velocities are shown in Figure 3. At 120 min, the flow rate was reduced to 66% in the artery and 55% in the vein. In addition, the peak flow rate was observed at 40 min after start of anesthesia for both the artery and vein. This is in line with previous observations on the effect of benzocaine on the central cardiovascular system and, therefore, we settled on applying the 40 min maximum flow velocity window in subsequent experiments in order to increase the chances of revealing all potential vessels in the ultrasound-based angiographies.

3.3. Neovascularization in the Spinal Cord Injury Site Evaluated with In Vivo Ultrasound Angiographies. Angiographies were successfully constructed for all axolotls at all time points. Figure 4 shows representative quadratic average processed angiographies at the SCI site for each treatment group at all time points. Variation in vessel volume fraction between groups and time points was analyzed using mixed ANOVA. Angiographies constructed at baseline were excluded in the calculations, since the spinous processes absorbed ultrasound waves, resulting in inconclusive values due to shadowing of the spinal cord vessels. The between-subject factor was group with three levels (sham, CSCI, and TSCI), and the within-subject factor was time with five levels (0, 3, 6, 12, and 63 DPI). A Bonferroni-corrected post hoc analysis was performed for the significant effects. Since the post hoc analysis compared four time points of the total subjects to 0 DPI, the Bonferroni-corrected level of significance was calculated to 0.0125.

We found no significant association between time and group ($p = 0.249$). However, a significant main effect of time

was observed ($p < 0.0001$). There was no significant main effect of the between-subject factor group ($p = 0.890$).

From the post hoc analysis, we found that mean vessel volume fraction of all subjects increased significantly from 0 to 63 DPI by 26.3% (95% CI = 11% : 42%; $p = 0.0002$).

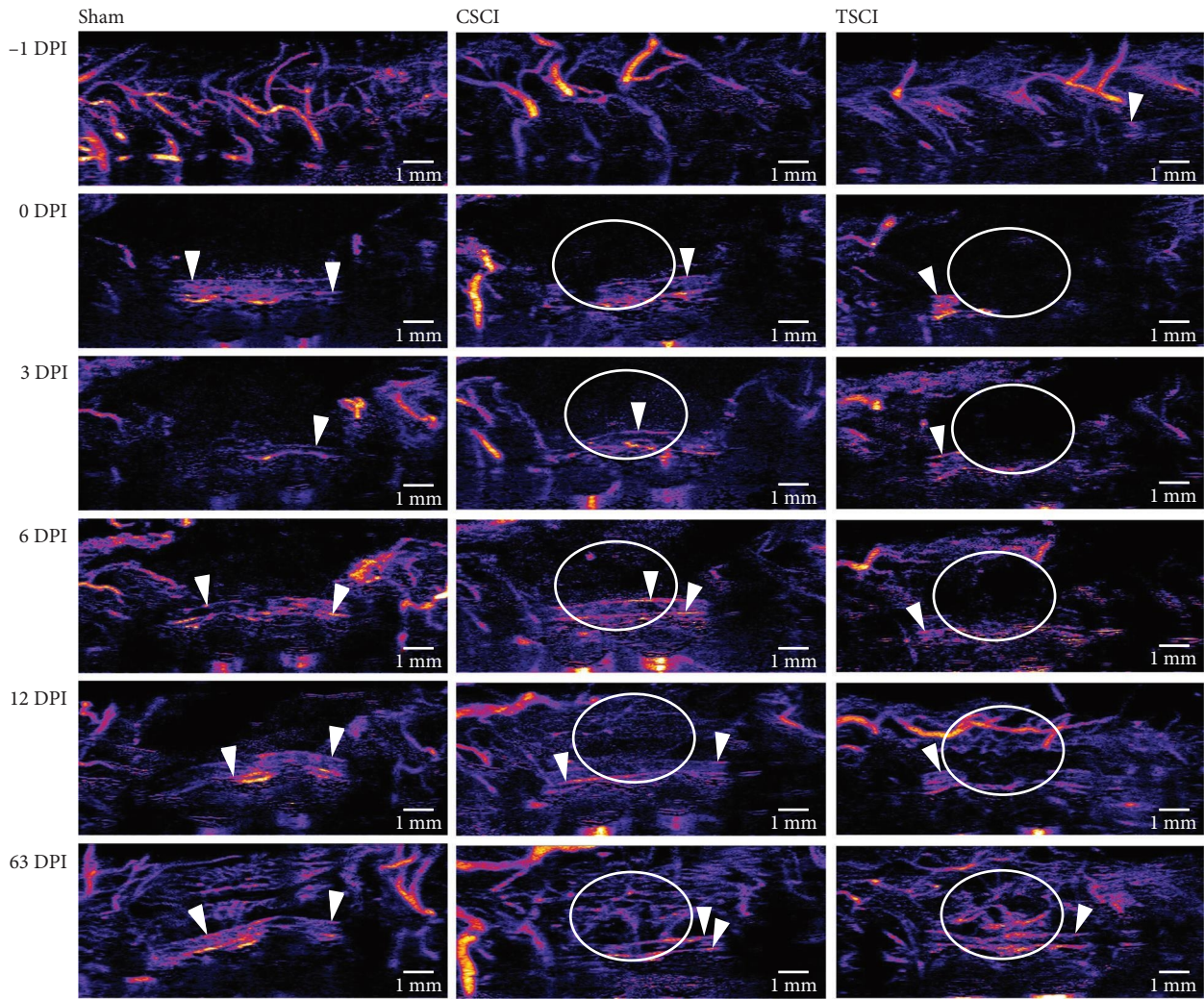
In conclusion, we found no differences between treatment groups, but we observed a significant increase in mean vessel volume fraction over time. This result suggests that neovascularization can be followed repeatedly and noninvasively by the postprocessing ultrasound method. The lack of difference between sham and the two injury groups indicates that the increased vessel volume fraction observed over time could be attributed to the surgical access itself and not the SCI per se. It is possible that the axolotl, due to its low metabolic nature, is less reliable on neovascularization into the SCI site compared to mammalian models to recover injured neurons.

3.4. Neovascularization in the Regenerating Spinal Cord Evaluated with Ex Vivo Contrast Agent-Based Micro-CT Imaging. All tail samples were successfully perfused with the microfil contrast agent. However, one sample was excluded due to leakage of microfil outside of the vascular system at the SCI site. Figure 5 shows representative micro-CT angiographies at the SCI site for each treatment group.

The analysis of differences between groups was computed as a one-way ANOVA, with the dependent variable being vessel volume fraction and the factor being group with three levels (sham, CSCI, TSCI). Bonferroni correction for three comparisons was applied, yielding a significance level of 0.017. The vessel volume fractions were found to be: sham: 3.1% (95% CI = 1.4% : 5.0%), CSCI: 2.3% (95% CI = 0.6% : 4%), and TSCI: 2.7% (95% CI = 0.1% : 5.6%). One-way ANOVA showed no significant effect of group ($p = 0.525$).

3.5. Visualization of Neurogenesis with Ex Vivo Contrast Agent-Enhanced Micro-CT Imaging and Histology. Evaluation of diceCT scanned and histological sections of end-point samples showed spinal cord regeneration across all treatment groups (Figures 6 and 7). In the sham-operated animals, no signs of SCI were observed (Figure 6, left column and Figure 7, left column). In the diceCT scans of the CSCI and TSCI animals, a coherent spinal cord was found in all animals, but with some remaining signs of SCI (hypodense areas) (Figure 6, middle and right columns). Similarly, in animals from the CSCI and TSCI groups, histology demonstrated a coherent spinal cord with some signs of injury such as a reduced overall spinal cord thickness with a widened central canal and disarranged spinal cord cells (Figure 7, middle and left columns). In diceCT scans, a dense network of vessels close to the injury site was observed in some of the TSCI animals (represented in Figure 6, lower right corner).

3.6. Neurologic Function Evaluated with Clinical Neurologic Examination. The sedentary lifestyle of the axolotl limits the use of nondisturbed behavioral observations to assess the degree of functional inhibition of the distal spinal cord after SCI. However, neurologic function can be tested by observing clinical signs after nociceptive and tactile stimuli to the



(a)

FIGURE 4: Continued.

tail. Animals subjected to sham showed an unaffected nociceptive response throughout the experiment (Figure 8(a)). In axolotls subjected to CSCI and TSCI, a decreased nociceptive response was observed, which was normalized at experimental end point (63 DPI) (Figure 8(a)). A decreased tactile response was observed in all groups (Figure 8(b)), indicating loss of tactile sensitivity due to the surgical intervention. The tactile response score reached normal values at experimental end point (63 DPI) (Figure 8(b)). We observed clonus-like movements after nociceptive stimuli in all groups. All axolotls subjected to TSCI, four subjected to CSCI, and only one sham axolotl displayed clonus-like movements.

3.7. Comparison between In Vivo Ultrasound and Ex Vivo Micro-CT. Figure 9 shows a Bland–Altman plot, illustrating the error between measurements of vessel volume fraction by ultrasound and micro-CT. Larger values of volume fraction tend toward yielding a higher difference between the two modalities, indicating systematic overestimation by ultrasound

or underestimation by micro-CT, and that this over/underestimation is dependent on the size of the volume measured. High-frequency ultrasound estimated the average vessel volume fraction of all samples to be 42.9% (95% CI=35.7%: 50.2%) at the end of the experiment, whereas micro-CT estimated it to be more than an order of magnitude lower at 2.75% (95% CI=2.07%: 3.42%), yielding a statistically significant difference ($p < 0.0001$) using a paired Student’s t -test.

In summary, we observed a significant difference in vessel volume fraction between the two modalities: ultrasound and micro-CT. Implied by the Bland–Altman plot, ultrasound-based angiographies may have overestimate the actual vessel volume fraction or micro-CT may have underestimated this. Ultrasound overestimation could be a result of small unnoticeable animal motions during the ultrasound scan, which enhances signal intensity in pixels in static soft tissue that is then erroneously added to the vessel volume. On the other hand, micro-CT underestimation could be due to incomplete filling of all minor capillaries with the contrast agent. This latter point was supported by transversal histology of the

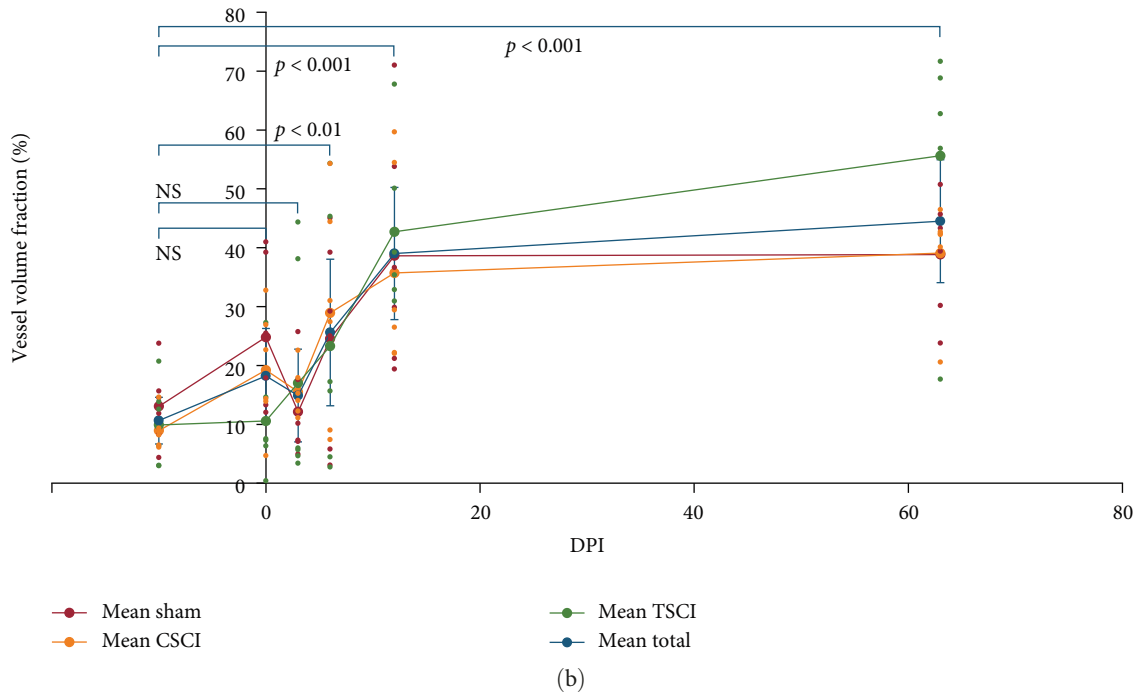


FIGURE 4: Neovascularization evaluated with ultrasound-based angiographies: (a) a series of processed cine image from one axolotl in each group. A lookup table (fire) was applied to highlight flow velocity differences; (b) plot illustrating the mean vessel volume fraction over time measured by high-frequency ultrasound. ANOVA showed that time is the only significant factor, hence a total of all groups were calculated. Blue: mean vessel volume fraction from all subjects. Error bars for total: Bonferroni corrected 95%-confidence intervals. Red: mean vessel volume fraction sham. Orange: mean vessel volume fraction CSCI. Green: mean vessel volume fraction TSCI. Small red, orange, and green points are individual data points. White arrowheads pointing at spinal cord blood vessels. White circles represent the SCI sites. Cranial side is to the right.

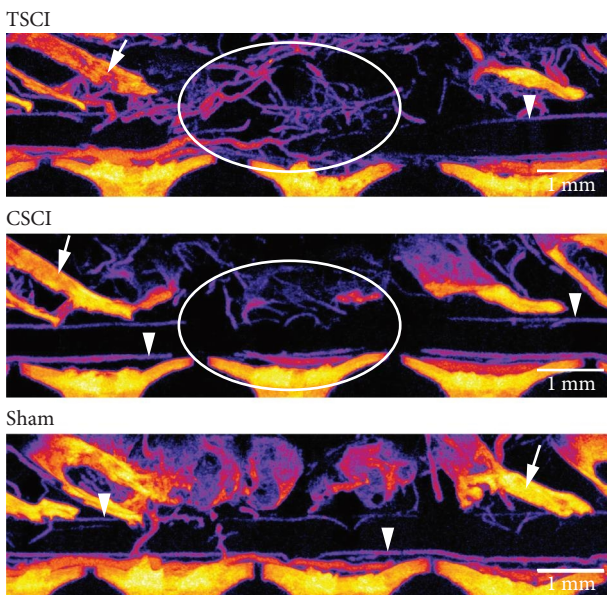


FIGURE 5: Contrast agent-enhanced micro-CT angiographies, showing one animal from each group at end point (63 DPI). White arrowheads point at spinal cord blood vessels, and white circles mark the SCI site. White arrows point at spinous processes. Cranial side is to the right.

spinal cord slightly caudal to the injury site (Figure 10). Quantitative analysis of these histology slices showed a vessel volume fraction of 11.9% (95% CI = 5.9% : 17.9%) comparable to the vessel volume fraction measured with ultrasound prior to injury (Figure 4). Additionally, analysis of transversal histology slices showed a microfil filling fraction of all vessel of 22.4% (95% CI = 11.6% : 33.2%), thus supporting incomplete vessel filling with microfil. In this sense, the ultrasound procedure is benefited by the fact that it is independent on contrast agent perfusion and all flowing blood is detected by the quadratic averaging procedure, and it is very likely that the significantly lower vessel volume fraction measurement with micro-CT in the injury zone is the result of incomplete contrast agent infusion.

The ultrasound procedure did not detect significant differences in vessel volume fraction between treatment groups although this may be expected. This could both be due to the biology of the regenerating spinal cord in the axolotl that perhaps there is no increase in vascularization associated with an injured and regenerating spinal cord, but it could also be explained by a lack of sensitivity of the ultrasound method. Contrast agent-enhanced micro-CT was only conducted at the experimental end point. Thus, we cannot conclude whether micro-CT could detect a difference before experimental end point. However, vessel volume fractions

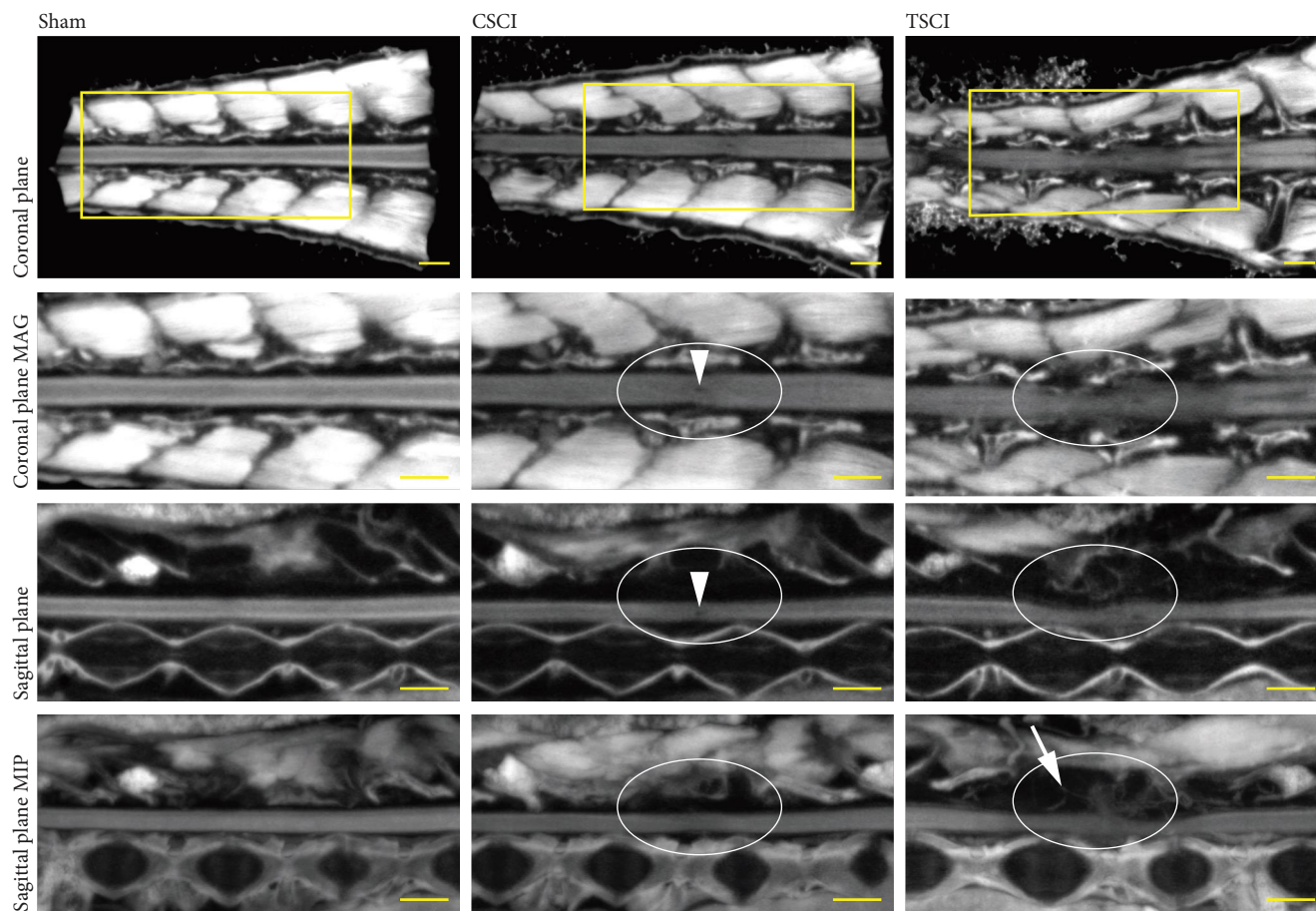


FIGURE 6: Diffusible iodine-based contrast-enhanced micro-CT evaluation of neurogenesis. Yellow boxes represent the magnified area. White arrowheads pointing at a hypodense area on the spinal cord. White arrow pointing at a sprouted vessel. White circles represent SCI sites. MAG, magnification; MIP, maximum intensity projection. Yellow scale bar in all panels represents 1 mm. Cranial side is to the right.

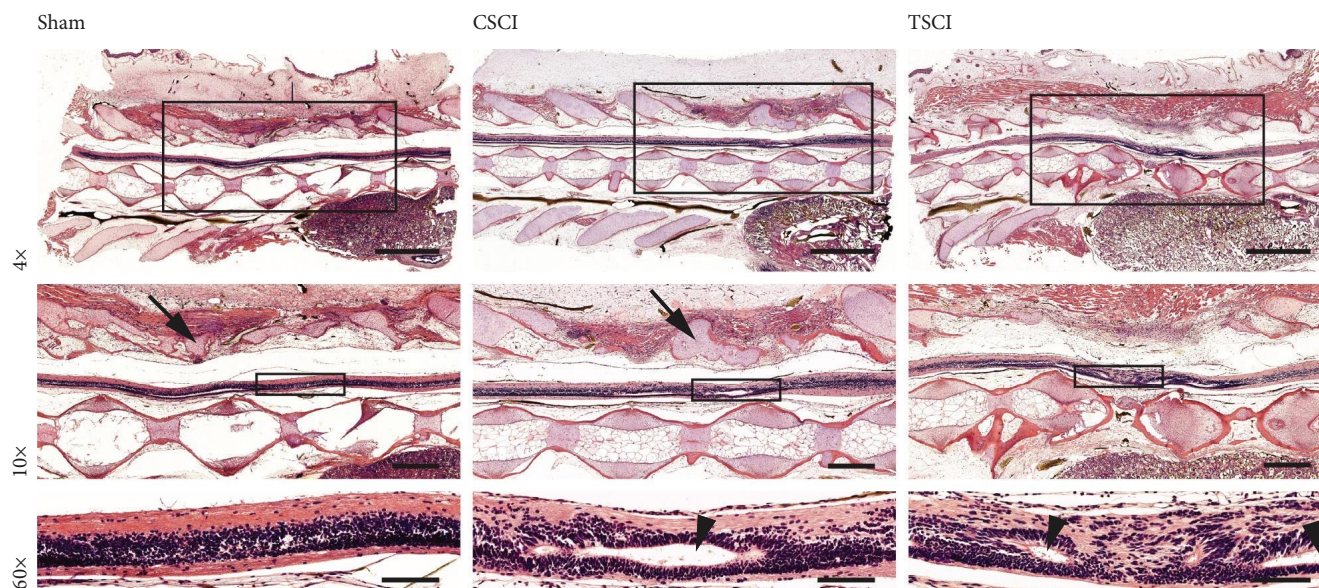


FIGURE 7: Visualization of the neurogenesis with histology (hematoxylin and eosin stained sections). One section from each group is represented. Black boxes represent the area that is magnified below. Black arrowheads point at the spinal cord central canal, which is dilated in the section from the CSCI sample and the TSCI sample. Black arrows point at the residual bones, which were not removed during the laminectomy. Scale bars: 4x, 2 mm; 10x, 1 mm; 60x, 200 μ m. Cranial side is to the right.

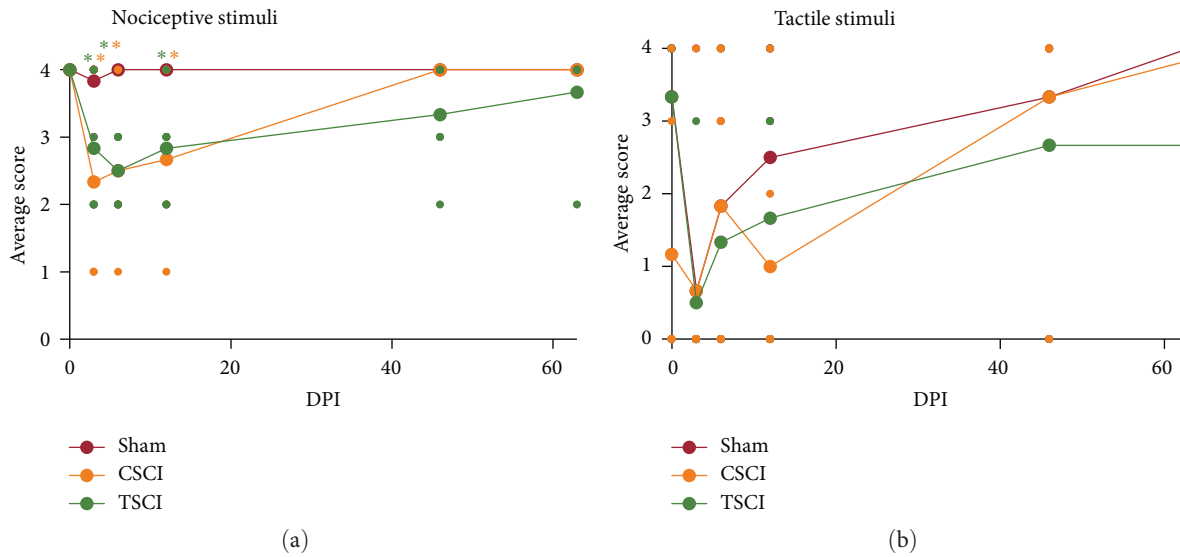


FIGURE 8: Neurologic function evaluated with clinical neurologic examination. (a) Graph showing results of nociceptive stimuli. Axolotls subjected to CSCI and TSCI have a markedly reduced response to nociceptive stimuli, whereas axolotls subjected to sham have a normal nociceptive response throughout the experiment. (b) Graph showing results of tactile stimuli. We observed a reduced tactile response in all groups, and the response was normalized at experimental end point (63 DPI). Small red, orange, and green points are individual data points. Colored asterisks indicate significant difference ($p < 0.05$) compared to sham.

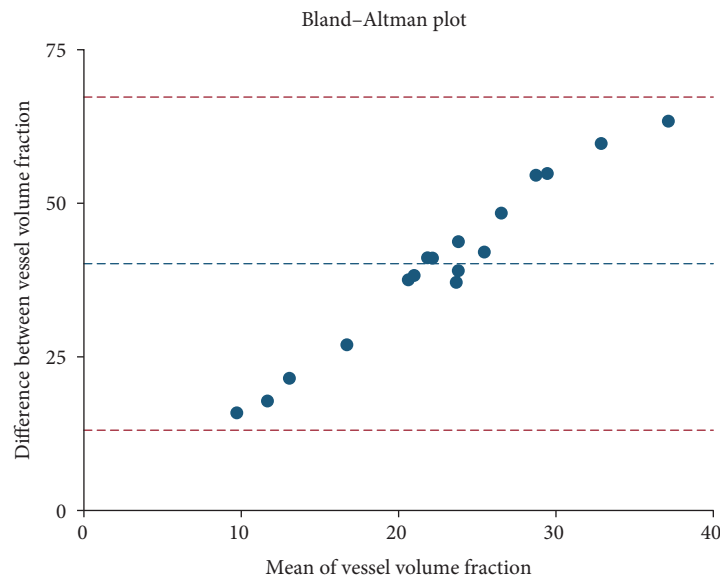


FIGURE 9: Comparison of the average vessel volume fractions calculated with micro-CT and high-frequency ultrasound at 63 DPI. Bland-Altman plot illustrating the association between the differences measured by the two modalities as a function of the mean of the measures by the two modalities. The plot suggests that the larger the actual volume vessel fraction is the larger is the difference between the two modalities.

based on micro-CT at the experimental end point showed no differences between the groups, offering support to the hypothesis that there was no difference between the groups.

4. Conclusion

In this study, we applied two different injury models, CSCI and TSCI, to the spinal cord of the regeneration competent axolotl salamander to demonstrate the application of a noninvasive *in vivo* evaluation of neovascularization using ultrasound. In addition to ultrasound, the injury response was evaluated

by micro-CT imaging (vascular contrast-enhanced and diceCT), histology, and clinical neurologic examination. We found that ultrasound-based angiographies using the procedure, originally developed by Tan et al. [1] and Dittrich et al. [2], could be applied to follow the neovascularization noninvasively and *in vivo* in the regenerating spinal cord in the axolotl. However, we found no correlation between signal intensities in quadratic averaged angiographies and flow velocities ruling out the option of applying the procedure to generate flow velocity maps. Second, we observed a significant increase in mean vessel volume fraction

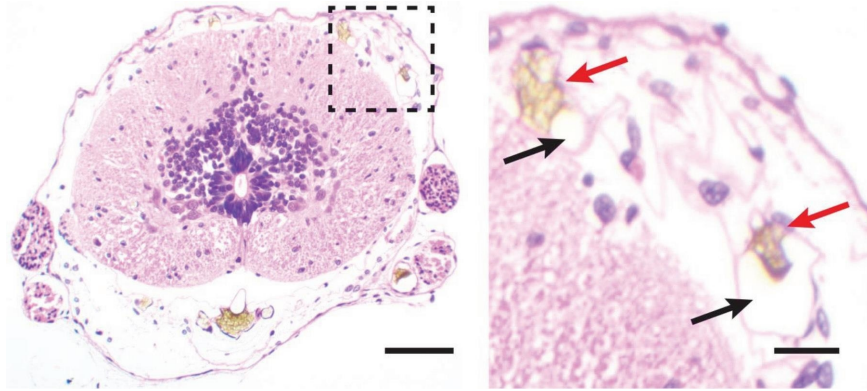


FIGURE 10: Representative cross-sectional slice of the spinal cord slightly caudal to the injury site. The micro-CT contrast agent microfil can be observed as yellow structures (red arrows). Many vessels show incomplete filling with microfil (black arrows). Image to the right is a magnification of the dashed box in the left image. Scale bars: left, 100 μm ; right, 25 μm .

over time. However, we observed no differences between groups, and the increase in vessel volume fraction could be attributable to the surgical intervention itself. Third, endpoint measurement comparison showed that vessel volume fractions based on ultrasound angiographies were significantly elevated compared to those based on micro-CT. These results implied an overestimation of vessel volume fractions based on ultrasound angiographies or more likely an underestimation by micro-CT due to the complications in delivering a contrast agent to minute capillaries, which was supported for histological evaluation. In overall, the results of this study suggest that noninvasive in vivo evaluation of neovascularization following SCI is possible in the regeneration competent axolotl salamander.

Data Availability

The raw ultrasound (620.4 GB) and micro-CT (46.4 GB) data used to support the findings of this study are available from the corresponding author upon reasonable request.

Conflicts of Interest

The authors declare that they have no conflicts of interest.

Funding

This study was funded by Helga og Peter Kornings Fond, Else og Mogens Wedell-Wedellsborgs Fond, The Lundbeck Foundation, The Novo Nordisk Foundation, and A.P. Møller Fonden.

Acknowledgments

We wish to thank Anita Dittrich for providing experimental support during surgery procedures.

Supplementary Materials

Script S1: macrosript that calculates the quadratic mean on a pixel by pixel basis of 1,000 frames ultrasound acquisition.

Implement in ImageJ in IJ1 macro language. (*Supplementary Materials*)

References

- [1] G. X. Y. Tan, M. Jamil, N. G. Z. Tee, L. Zhong, and C. H. Yap, "3D reconstruction of chick embryo vascular geometries using non-invasive high-frequency ultrasound for computational fluid dynamics studies," *Annals of Biomedical Engineering*, vol. 43, no. 11, pp. 2780–2793, 2015.
- [2] A. Dittrich, M. M. Thygesen, and H. Lauridsen, "2D and 3D echocardiography in the axolotl (*Ambystoma mexicanum*)," *Journal of Visualized Experiments*, no. 141, Article ID e57089, 2018.
- [3] C. Damsgaard and H. Lauridsen, "Deep vascular imaging in the eye with flow-enhanced ultrasound," *Journal of Visualized Experiments*, no. 176, Article ID e62986, 2021.
- [4] B. B. Lee, R. A. Cripps, M. Fitzharris, and P. C. Wing, "The global map for traumatic spinal cord injury epidemiology: update 2011, global incidence rate," *Spinal Cord*, vol. 52, pp. 110–116, 2014.
- [5] B. Bjørnshave Noe, E. M. Mikkelsen, R. M. Hansen, M. Thygesen, and E. M. Hagen, "Incidence of traumatic spinal cord injury in Denmark, 1990–2012: a hospital-based study," *Spinal Cord*, vol. 53, no. 6, pp. 436–440, 2015.
- [6] S. B. Jazayeri, S. Beygi, F. Shokraneh, E. M. Hagen, and V. Rahimi-Movaghar, "Incidence of traumatic spinal cord injury worldwide: a systematic review," *European Spine Journal*, vol. 24, no. 5, pp. 905–918, 2015.
- [7] J. C. Furlan, B. M. Sakakibara, W. C. Miller, and A. V. Krassioukov, "Global incidence and prevalence of traumatic spinal cord injury," *Canadian Journal of Neurological Sciences*, vol. 40, no. 4, pp. 456–464, 2013.
- [8] H. Binder, "Traumatic spinal cord injury," in *Handbook of Clinical Neurology*, vol. 110, pp. 411–426, Elsevier, 2013.
- [9] R. Sweis and J. Biller, "Systemic complications of spinal cord injury," *Current Neurology and Neuroscience Reports*, vol. 17, Article ID 8, 1910.
- [10] S. Yu, S. Yao, Y. Wen, Y. Wang, H. Wang, and Q. Xu, "Angiogenic microspheres promote neural regeneration and motor function recovery after spinal cord injury in rats," *Scientific Reports*, vol. 6, Article ID 33428, 2016.
- [11] J. Hu, Y. Cao, T. Wu, D. Li, and H. Lu, "Micro-CT as a tool to investigate the efficacy of tetramethylpyrazine in a rat spinal cord injury model," *Spine*, vol. 41, no. 16, pp. 1272–1278, 2016.

- [12] J. J. Herrera, L. M. Sundberg, L. Zentilin, M. Giacca, and P. A. Narayana, "Sustained expression of vascular endothelial growth factor and angiopoietin-1 improves blood-spinal cord barrier integrity and functional recovery after spinal cord injury," *Journal of Neurotrauma*, vol. 27, no. 11, pp. 2067–2076, 2010.
- [13] R. Muramatsu, C. Takahashi, S. Miyake, H. Fujimura, H. Mochizuki, and T. Yamashita, "Angiogenesis induced by CNS inflammation promotes neuronal remodeling through vessel-derived prostacyclin," *Nature Medicine*, vol. 18, no. 11, pp. 1658–1664, 2012.
- [14] J. J. O'hab, S. Fleming, A. Blesch, and S. T. Carmichael, "A neurovascular niche for neurogenesis after stroke," *Journal of Neuroscience*, vol. 26, no. 50, pp. 13007–13016, 2006.
- [15] A. Tazaki, E. M. Tanaka, and J.-F. Fei, "Salamander spinal cord regeneration: the ultimate positive control in vertebrate spinal cord regeneration," *Developmental Biology*, vol. 432, no. 1, pp. 63–71, 2017.
- [16] J. B. Armstrong and G. M. Malacinski, *Developmental Biology of the Axolotl*, Oxford University Press, New York, 1989.
- [17] J. Gresens, "An introduction to the Mexican axolotl (*Ambystoma mexicanum*)," *Lab Animal*, vol. 33, no. 9, pp. 41–47, 2004.
- [18] S. Roy and S. Gatien, "Regeneration in axolotls: a model to aim for!," *Experimental Gerontology*, vol. 43, no. 11, pp. 968–973, 2008.
- [19] M. M. Thygesen, H. Lauridsen, M. Pedersen, D. Orłowski, T. W. Mikkelsen, and M. M. Rasmussen, "A clinically relevant blunt spinal cord injury model in the regeneration competent axolotl (*Ambystoma mexicanum*) tail," *Experimental and Therapeutic Medicine*, vol. 17, no. 3, pp. 2322–2328, 2019.
- [20] J. Schindelin, I. Arganda-Carreras, E. Frise et al., "Fiji: an open-source platform for biological-image analysis," *Nature Methods*, vol. 9, no. 7, pp. 676–682, 2012.
- [21] M. M. Thygesen, M. M. Rasmussen, J. G. Madsen, M. Pedersen, and H. Lauridsen, "Propofol (2,6-diisopropylphenol) is an applicable immersion anesthetic in the axolotl with potential uses in hemodynamic and neurophysiological experiments," *Regeneration*, vol. 4, no. 3, pp. 124–131, 2017.